Available online at www.sciencedirect.com

ScienceDirect

Geochimica et Cosmochimica Acta 304 (2021) 347–363

Geochimica et Cosmochimica Acta

www.elsevier.com/locate/gca

Hydrodynamic processes and source changes caused elevated ^{14}C ages of organic carbon in the East China Sea over the last 14.3 kyr

Hailong Zhang [a], Da-Wei Li [a,b,*], Julian P. Sachs [c], Zineng Yuan [a], Zicheng Wang [a], Chenglong Su [a], Meixun Zhao [a,b,*]

[a] *Frontiers Science Center for Deep Ocean Multispheres and Earth System, and Key Laboratory of Marine Chemistry Theory and Technology, Ministry of Education, Ocean University of China, Qingdao 266100, China*

[b] *Laboratory for Marine Ecology and Environmental Science, Qingdao National Laboratory for Marine Science and Technology, Qingdao 266237, China*

[c] *School of Oceanography, University of Washington, Box 355351, Seattle, WA 98198, USA*

Received 14 August 2020; accepted in revised form 7 April 2021; Available online 20 April 2021

Abatract

More than 80% of marine organic carbon (OC) burial occurs in sediments of marginal seas. Sedimentary OC ^{14}C ages up to several millennia older than co-deposited coastal and pelagic sediments have been well documented but the cause of this phenomenon remains uncertain. We measured ^{14}C and ^{13}C contents of OC, along with the sedimentary content of terrestrial and marine lipid biomarkers, in sediment cores from the East China Sea to evaluate and quantify processes controlling OC ages over the last 14.3 kyr. We find that ^{14}C ages of OC were persistently older than co-deposited sediments by 1930–5530 yr. Temporal variations of the calculated apparent initial radiocarbon ages of total OC (TOC-AIR) mirrored sea level changes, with higher values (4570 ± 1250 yr) during the transgression (14.1–7.8 kyr BP) and lower values (3170 ± 670 yr) during the mid-late Holocene (7.8–0 kyr BP), suggesting that transgression-induced coastline retreat reduced the transport of pre-aged terrestrial OC to the marginal sea. However, bulk OC ^{14}C ages were consistently older than those expected from ternary mixing of Changjiang (Yangtze River), Huanghe (Yellow River) and marine sources based on $\delta^{13}C$ and $\Delta^{14}C$ end-members. We therefore propose that hydrodynamic processes during sediment transport and the addition of pre-aged OC from land and submerged coast were the main factors contributing to these old ^{14}C ages of OC and their temporal variations. During the transgression, higher TOC-AIR values were observed during times of lower sea-level, which suggests that erosion of coastal deposits during transgression might have contributed old OC. Since sea level stabilized 7.8 kyr BP hydrodynamic processes were the primary cause of high ^{14}C ages of OC. The significant role for hydrodynamic aging processes during the mid-late Holocene is hypothesized to result from longer transport distances between river mouths and sediment depocenters which can accommodate additional deposition-resuspension loops.

Keywords: East China Sea; Holocene; Organic carbon source and burial; Radiocarbon age; Hydrodynamic process aging

* Corresponding authors at: Frontiers Science Center for Deep Ocean Multispheres and Earth System, and Key Laboratory of Marine Chemistry Theory and Technology, Ministry of Education, Ocean University of China, Qingdao 266100, China.

E-mail addresses: ldw@ouc.edu.cn (D.-W. Li), maxzhao@ouc.edu.cn (M. Zhao).

https://doi.org/10.1016/j.gca.2021.04.015

1. INTRODUCTION

Photosynthetic removal of CO_2 from the atmosphere and the subsequent burial of organic carbon (OC) in seafloor sediments plays a central role in modulating long-term carbon cycling and climate (Hedges et al., 1997; Burdige, 2005). For example, the OC burial in marine sediments may have increased by ca. 50% during glacial periods (e.g., excess burial of 200–500 Pg C of OC) relative to interglacial periods (Cartapanis et al., 2016), an amount of carbon equivalent to the 80–100 ppm reduction of atmospheric CO_2 during glacial periods (Sigman and Boyle, 2000). Sedimentary OC is comprised of marine OC that is rapidly transported to the seafloor and buried, pre-aged terrestrial (or marine) carbon fixed hundreds to thousands of years before burial, and fossil carbon (zero ^{14}C activity, or dead carbon) derived from sedimentary rocks (Blair et al., 2003; Galy et al., 2008; Drenzek et al., 2009). Burial of contemporary and pre-aged OC contributes to atmospheric CO_2 declines on millennial timescales, but burial of fossil OC does not (Leithold et al., 2016 and references therein). On the contrary, degradation of all three OC age fractions releases CO_2 to the ocean–atmosphere system (Blair and Aller, 2012; Leithold et al., 2016). Understanding the role of sediment OC burial in regulating atmospheric CO_2 over time requires a better knowledge of the OC composition and ages from different geographic areas, particularly marginal seas where 80% of marine OC is buried (Burdige, 2005).

Shallow and broad marginal seas represent important mixing zones between land and ocean where vast quantities of terrestrial and in situ-produced marine OC are recycled and buried. Numerous studies have shown that OC in surface sediments from global marginal seas (including the Chinese marginal seas) spans a wide range of radiocarbon ages, from modern to 10^4 yr (Griffith et al., 2010 and references therein; Bao et al., 2016). Radiocarbon ages of OC ($^{14}C_{org}$ ages) deposited from the last glacial maximum to late Holocene are older than ^{14}C ages of co-deposited planktonic foraminifera by hundreds to thousands of years on and adjacent to continental margins in the Pacific Ocean including the South China Sea (Mollenhauer et al., 2005), the Southern Chile slope (Mollenhauer et al., 2005), the Okinawa Trough (Kao et al., 2008), and the Waipaoa River estuary in New Zealand (Leithold et al., 2013); in the Atlantic Ocean including the Namibian margin (Mollenhauer et al., 2005), Congo River basin (Schefuß et al., 2016), Iberian margin (Ausín et al., 2019), and Bermuda Rise (Ohkouchi et al., 2002); and in the Ganges-Brahmaputra delta of the Indian Ocean (Hein et al., 2020). These spatiotemporal age offsets were explained by changes in the relative proportion of autochthonous OC (i.e., in situ marine production) and terrestrial inputs of pre-aged and fossil OC. More recently the additional role of apparent OC aging during hydrodynamic processes has been identified as being important in causing high ^{14}C ages of OC relative to coeval surface sediments (Mollenhauer et al., 2007; Bao et al., 2018a; Bröder et al., 2018; Wei et al., 2020).

The East China Sea (ECS) accounts for less than 0.2% of the world's ocean area but its OC burial flux (7.4 Tg C yr^{-1}) accounts for more than 4% of the global total (160 Tg C yr^{-1}) (Burdige, 2005; Jiao et al., 2018). It receives large quantities of terrestrial material from the Huanghe (Yellow River) and Changjiang (Yangtze River) (Milliman et al., 1985; Liu et al., 2003; Li et al., 2012; Hu et al., 2014; Dou et al., 2015) and has been shown to have OC in surface sediments characterized by $^{14}C_{org}$ ages ranging between 1605–2750 yr in the Southwestern Cheju Island Mud (SWCIM, see yellow area in Fig. 1) of the ECS to 16,400 yr north of Taiwan (Wu et al., 2013; Bao et al., 2016). This implies a substantial proportion of pre-aged or fossil OC is incorporated into ECS sediments. By using a mixing model constrained by the $\delta^{13}C$ and $\Delta^{14}C$ values of bulk OC, Bao et al. (2018b) concluded that variations of terrestrial and marine sources could not fully explain the old $^{14}C_{org}$ ages and proposed that hydrodynamic processes such as repeated deposition-resuspension loops during lateral transport and preferential removal of labile OC likely played a role. This hydrodynamic aging process has been proposed to occur in other continental margin settings such as the Yellow Sea (Bao et al., 2018a), South China Sea (Wei et al., 2020), Washington margin (Bao et al., 2018a), East Siberian Arctic shelf (Bröder et al., 2018), and Namibian margin (Mollenhauer et al., 2007).

Lipid biomarker records from the ECS indicate significant changes in the relative proportion of terrestrial and marine OC since the last deglaciation (Yuan et al., 2013; Wang et al., 2019) that would be expected to cause variations in $^{14}C_{org}$ ages, but as of yet such changes have not been documented. Southeast of the ECS in the southern Okinawa Trough, Kao et al. (2008) reported $^{14}C_{org}$ ages during the last glacial maximum (LGM) that were 2660 yr older than co-deposited planktonic foraminifera, and the age offset increased to 7390 yr in the mid-Holocene. They concluded that this temporal change resulted from an enhanced supply of fossil OC associated with sea level rise. Other studies have shown that pre-aged OC deposited in the ECS shelf gets laterally advected into the Okinawa Trough (Honda et al., 2000), resulting in hydrodynamic aging of OC (Bao et al., 2019b). The Okinawa Trough $^{14}C_{org}$ ages since the LGM reported by Kao et al. (2008) are therefore likely to include the imprint of the hydrodynamic aging process.

In this study, the $\delta^{13}C$ and $\Delta^{14}C$ values of bulk OC and the sedimentary contents of a suite of lipid biomarkers were measured in three sediment cores from the SWCIM of the central ECS spanning the past 14.3 kyr in an effort to quantify and understand temporal variations of $^{14}C_{org}$ ages and composition during the glacial-interglacial transition. Results of this study provide insights into the processes controlling OC burial in Chinese marginal seas and other similar depositional settings, with implications for global carbon cycling and atmospheric CO_2 levels.

2. MATERIAL AND METHOD

2.1. Study area

The ECS is one of the largest marginal seas in the western North Pacific Ocean with the Eurasian continent to the

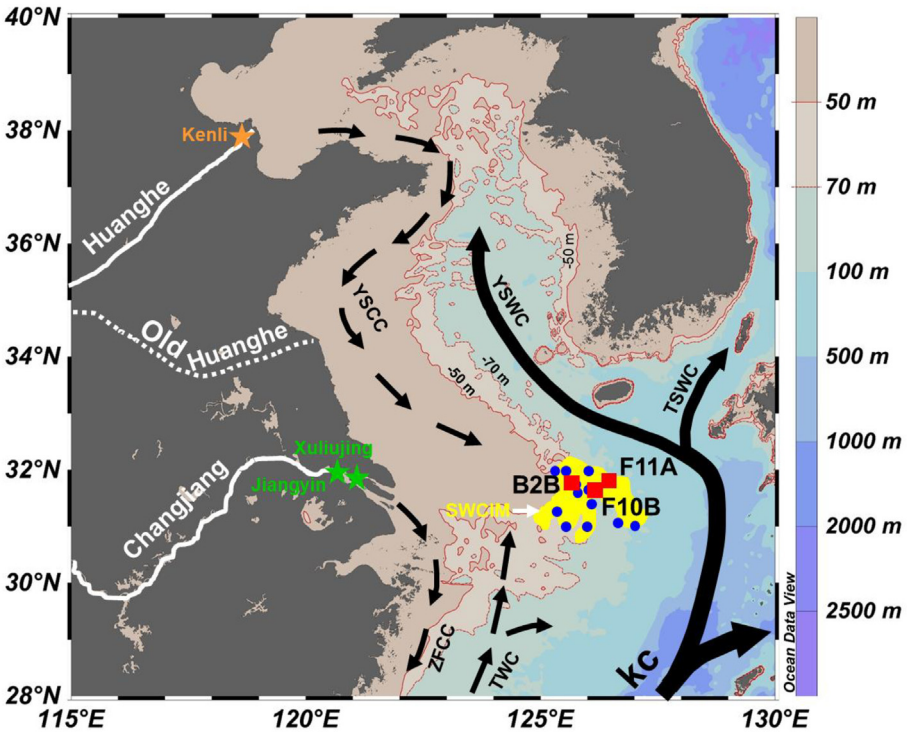

Fig. 1. Locations of F10B, F11A cores ■) and surface sediment sites referred in this study. The yellow area represents Southwestern Cheju Island Mud (SWCIM) redrawn from Li et al. (2014). The −50 m and −75 m isobaths are shown by the dashed red lines. Sites of surface sediments in the SWCIM ●) are from Bao et al. (2016). Stars (★ and★) represent river hydrological stations mentioned in this study. The currents include: KC, Kuroshio Current; YSWC, Yellow Sea Warm Current; YSCC, Yellow Sea Coastal Current; TSWC, Tsushima Warm Current; ZFCC, Zhejiang-Fujian Coastal Current; TWC, Taiwan Warm Current.

west and the Okinawa and Ryukyu Islands to the east. It is characterized by a broad continental shelf that receives vast quantities of detritus from the large Changjiang and Huanghe, and smaller rivers in Taiwan and the Korean Peninsula (Li et al., 2012). Both coastal and tidal currents control sediment transport and deposition (Bian et al., 2013). Today (and during the mid-late Holocene) tidal-current intensity is relatively weak in regions to the southwest of Cheju Island and below the threshold for initiating movement of fine-particles (Uehara and Saito, 2003). Fine grained sediments from the Changjiang and Huanghe are instead dispersed by coastal and off-shore currents and deposited in the >10,000 km^2 central ECS region referred to as the SWCIM; 30.87°N – 32.15°N, 125.07° E – 127.05°E) (Li et al., 2014). Continuous sediment deposition has occurred in the SWCIM since at least 14 kyr ago (Hu et al., 2014; Kim and Lim, 2014; Wang et al., 2019), with mostly fine-grained muds deposited since 7–8 kyr ago (Kim and Lim, 2014; Li et al., 2014). Today, the SWCIM is considered the distal end of the Huanghe dispersal system, with Huanghe-derived sediment transported to the SWCIM by China coastal currents (DeMaster et al., 1985; Alexander et al., 1991; Yuan et al., 2008). Sediments from the Changjiang tend to be deposited on the inner shelf and transported south by the Zhejiang-Fujian Coastal Current (ZFCC in Fig. 1) (Yang et al., 2016 and references therein). The marine transgression during the deglacial and early Holocene caused westward movements of paleo-river estuaries (Li et al., 2014) that fundamentally altered the amount and character of terrestrial OC entering the ECS and the associated sediment transport pathways (Yuan et al., 2013; Hu et al., 2014; Dou et al., 2015). For example, sedimentologic and mineralogic studies indicate that the majority of sediments delivered to the SWCIM were from the Huanghe during the mid-late Holocene (Yuan et al., 2008; Zhou et al., 2014; Dou et al., 2015; Yang et al., 2016), whereas increased contribution from the Changjiang (Dou et al., 2015) or paleo-coastal erosion (Hu et al., 2014) occurred during the transgression. Therefore, sediment cores in the SWCIM provide good archives to investigate the responses of OC sources and ages to sea level change.

2.2. Sediment cores and age model

Gravity cores B2B (249 cm length; water depth 61 m; 125.75°E, 31.75°N), F10B (141 cm length; water depth 79 m; 31.73°N, 126.12°E) and F11A (206 cm length; water depth: 93 m; 31.88°N, 126.35°E) were recovered in 2011 by the R/V *Dongfanghong II* (see Fig. 1 for core sites) from the west, middle and east of the SWCIM. The age models for three cores are based on AMS ^{14}C data of mixed benthic foraminifera, in which the foraminiferal AMS ^{14}C data for cores F10B and F11A haven been reported by Xing et al. (2013) and Yuan et al. (2018), respectively. For core B2B, new foraminiferal AMS ^{14}C data have been obtained

Table 1
The AMS ^{14}C ages and calendar ages of core B2B.

Depth (cm)	Dating material	AMS ^{14}C Fm	AMS ^{14}C age (yr BP)	Calendar age (cal yr BP)	2σ error range (cal yr BP)
42–44	Mixed benthic foraminifera	0.8802 ± 0.0022	1025 ± 20	701	636–782
82–84	Mixed benthic foraminifera	0.8292 ± 0.0021	1505 ± 20	1200	1092–1279
122–124	Mixed benthic foraminifera	0.7983 ± 0.0020	1810 ± 20	1486	1376–1593
162–164	Mixed benthic foraminifera	0.7738 ± 0.0019	2060 ± 20	1784	1676–1892
202–204	Mixed benthic foraminifera	0.7454 ± 0.0019	2360 ± 20	2152	2030–2288
240–244	Mixed benthic foraminifera	0.7137 ± 0.0022	2710 ± 25	2601	2450–2719

Notes: Fm is $\delta^{13}C$-normalized fraction modern.

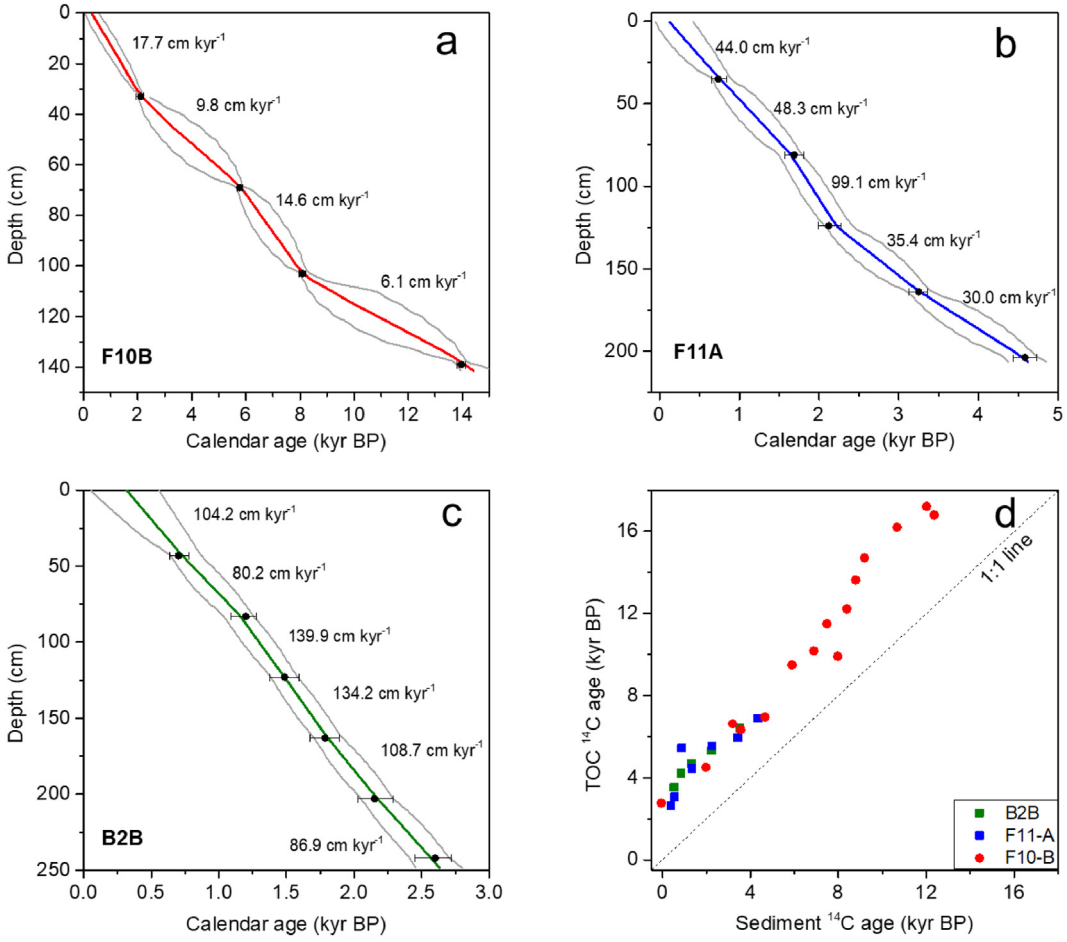

Fig. 2. Radiocarbon ages of benthic foraminifera and TOC. Age-depth plots based on sediment AMS ^{14}C calendar ages (black solid dots) for cores (a) F10B, (b) F11A, and (c) B2B cores. Linear sediment accumulation rates are indicated in each panel. Error bars denote the two sigma (2σ) uncertainty of the ^{14}C calendar ages, and gray lines refer to the 2σ age uncertainty derived from the Bayesian statistical age modeling software Bacon. (d) A plot of $^{14}C_{org}$ ages versus sediment ^{14}C ages. Sediment ^{14}C age was calculated by interpolation between benthic foraminiferal ^{14}C age points using the Bayesian age-depth model.

(Table 1). We refer to the Appendix A for a detailed discussion of the age model for core F10B. By using Marine13 in the CALIB 7.1 program (Reimer et al., 2013), AMS ^{14}C ages were calibrated to calendar ages (BP, relative to 1950 CE; black solid rectangles in Fig. 2a-2c) with a regional marine reservoir age correction ($\Delta R = -128 \pm 35$ yr) (Zhong et al., 2018). Age models for samples of the three cores were established using the Bacon software (version 2.3.4; Blaauw and Christen, 2011). Core F10B (0–141 cm) spans the period 0.3–14.3 kyr BP (Fig. 2a), core F11A (0–206 cm) spans the period 0.1–4.6 kyr BP (Fig. 2b) and core B2B (0–249 cm) spans the period 0.3–2.6 kyr BP (Fig. 2c). As shown in Fig. 2, the three cores have linear sedimentation rates that differ by 1 to 2 orders of magnitude. Composite results from the three cores were therefore considered most representative of OC radiocarbon age

changes in the SWCIM, especially during the mid-late Holocene.

2.3. Analyses of organic carbon content and its isotope composition

Sediment samples were taken at 1–4.5 cm intervals between 3 cm and 137 cm in core F10B (75 samples) and at 1 to 2 cm intervals between 0 cm and 206 cm in core F11A (104 samples) and at five depths of 0–1 cm, 26–27 cm, 66–67 cm, 186–187 cm and 248–249 cm in core B2B. For TOC and $\delta^{13}C$ analyses, sediments were then freeze dried and carbonate was removed by adding 4 N HCl. Sediments were subsequently rinsed with Milli-Q water repeatedly until a pH of 7 was reached, then centrifuged to remove water and oven-dried at 50 °C. Approximately 5–30 mg of the dried, decarbonated sediment was placed in a ceramic boat and analyzed for TOC content with an Elemental Analyzer FLASH 2000 at Ocean University of China with a standard deviation of ± 0.02 wt% (n = 6), determined by replicate analysis of atropine (Thermo Fisher Scientific, Netherlands) and a low organic content soil (Elemental Microanalysis Ltd., UK). Another aliquot of 5–30 mg of the dried sample was placed in a ceramic boat and analyzed for TOC $\delta^{13}C$ on EA-IRMS (FLASH EA 1112 series coupled with Thermo Fisher Delta V isotopic ratio mass spectrometer) at Ocean University of China. Measured $\delta^{13}C$ values were calibrated against carbon isotope standards USGS 40 ($\delta^{13}C = -26.39‰$ vs. Vienna Pee Dee Belemnite, VPDB), IAEA 600 ($\delta^{13}C = -27.77‰$ vs. VPDB) and IAEA-CH3 ($\delta^{13}C = -24.72‰$ vs. VPDB) and a laboratory working standard ($\delta^{13}C = -23.8‰$ vs. VPDB). The $\delta^{13}C$ measurement standard deviation is less than ±0.1‰ (n = 6) determined by replicate analyses of USGS 40, IAEA 600 and a laboratory working standard.

Fifteen samples from core F10B, seven samples from core F11A and five samples from core B2B were analyzed for TOC ^{14}C at the National Ocean Sciences Accelerator Mass Spectrometry Facility (NOSAMS) at the Woods Hole Oceanographic Institution (McNichol et al., 1994; Pearson et al., 1997). Prior to AMS analysis, fumigation was carried out for sediments in the presence of HCl (37%, 72 hr) to remove carbonate, and excess HCl was removed by drying over NaOH pellets (72 hr) in a desiccator at 60 °C. The radiocarbon content of TOC was reported as fraction modern (Fm, Table 2). The initial radiocarbon content ($\Delta^{14}C_{initial}$) at the time of sediment deposition was calculated from the measured Fm using the equation by Schefuß et al. (2016):

$$\Delta^{14}C_{initial} = (Fm \times e^{\lambda t} - 1) \times 1000‰ \quad (1)$$

where Fm is the measured fraction modern of the sample, λ is the radiocarbon decay constant (1/8267 yr^{-1}), and t is time since deposition in years constrained by calibrated benthic foraminifera ages. Considering the variation of atmospheric radiocarbon content ($\Delta^{14}C_{atm}$) and assuming the shallow ECS was well mixed and equilibrated with CO_2 in the atmosphere, the apparent initial radiocarbon ages of TOC (TOC-AIR) at the time of sediment deposition and $\Delta\Delta^{14}C_{org}$ (i.e., the offset between initial radiocarbon contents of OC, i.e., $\Delta^{14}C_{initial}$, and that of the past atmosphere, i.e., $\Delta^{14}C_{atm}$) are calculated using the following equations:

$$AIR = -8033 \times \ln[(1+\Delta^{14}C_{initial}/1000)/(1+\Delta^{14}C_{atm}/1000)] \quad (2)$$

$$\Delta\Delta^{14}C_{org} = \Delta^{14}C_{initial} - \Delta^{14}C_{atm} \quad (3)$$

where $\Delta^{14}C_{initial}$ is the initial radiocarbon content of OC calculated using equation (1) and $\Delta^{14}C_{atm}$ (from the Intcal13 Northern Hemisphere atmospheric data) is the atmospheric radiocarbon content at the time of sediment deposition (Reimer et al., 2013).

2.4. Analyses of glycerol dibiphytanyl glycerol tetraethers (GDGTs)

GDGTs were extracted from sediment according to procedures described by Xing et al. (2013). Briefly, 2–5 g freeze-dried samples were ultrasonically extracted 4 times with a mixture of methanol and dichloromethane (v/v = 1:3) after adding 0.5 μg C_{46} GDGT as an internal standard. The extracts were hydrolyzed in a 6% KOH-methanol solution at room temperature for 12 hr before neutral components were extracted with *n*-hexane. Then, the neutral components were further separated into apolar and polar fractions (containing GDGTs) through activated silica gel chromatography using *n*-hexane and dichloromethane/methanol (v/v = 95:5) as eluents, respectively. The polar fraction was filtered through a PTFE membrane (0.45 μm) before injecting into an HPLC-MSMS (Agilent 1200/Waters Micromass-Quattro Ultima™ Pt) according to procedures in Li et al. (2013). Semi-quantification of GDGTs was performed by comparing individual peak areas to that of the C_{46} GDGT internal standard. Duplicate measurements resulted in a precision better than 10%.

2.5. Analyses of mineral-specific surface area (SA)

About 1 g freeze-dried samples were heated at 350 °C for 12 hr to remove organic matter (Mayer, 1994). Then, mineral-specific SA was measured by a 5-point BET method using NOVA 4000 SA analyzer (Quantachrome Instrument) at Ocean University of China.

3. RESULTS

3.1. Organic carbon and GDGT content

The TOC content of sediments in core F11A was between 0.46% and 0.87% (wt) (Fig. 3a, blue). It increased gradually from ca. 0.55% at 4.6 kyr BP to ca. 0.76% at 3.0 kyr BP, before decreasing gradually to 0.60% at 1.2 kyr BP, and finally rising rapidly to 0.87% at 0.4 kyr BP. Five TOC values in core B2B varied within a narrow range of 0.56%–0.76% (Fig. 3a, green). TOC content in core F10B varied between 0.13% and 0.77%. It was relatively low from 14.0 – 5.8 kyr BP (Fig. 3a, red), then increased gradually from 0.31% at 5.6 kyr BP to 0.77% at 0.8 kyr BP. Within

Table 2
Carbon isotopes and radiocarbon ages for total organic carbon (TOC) samples in core F11A, B2B and F10B.

Sediment			TOC					
core	Depth (cm)	Calibration age (yr 1950 BP)	Fm	$\Delta^{14}C_{initial}$ (‰)	^{14}C age (yr)	$\Delta\Delta^{14}C_{org}$ (‰)	AIR (yr)	$\delta^{13}C$ (‰)
F11A	0–1	130 ± 137	0.7213 ± 0.0015	−267 ± 12	2624 ± 17	−264 ± 12	2476 ± 134	−21.1
	8–9	275 ± 130	0.6828 ± 0.0013	−294 ± 11	3065 ± 15	−300 ± 11	2847 ± 127	−21.0
	24–25	567 ± 102	0.5075 ± 0.0042	−456 ± 8	5448 ± 66	−454 ± 8	4877 ± 120	−20.9
	48–49	1021 ± 114	0.5743 ± 0.0013	−350 ± 9	4455 ± 18	−334 ± 9	3331 ± 113	−21.1
	112–113	2066 ± 92	0.5016 ± 0.0012	−356 ± 7	5542 ± 19	−346 ± 7	3451 ± 92	−21.1
	170–171	3480 ± 129	0.4768 ± 0.0012	−274 ± 11	5950 ± 20	−289 ± 12	2690 ± 127	−21.1
	205–206	4597 ± 104	0.4237 ± 0.0019	−261 ± 10	6898 ± 36	−303 ± 10	2763 ± 108	−21.3
B2B	0–1	322 ± 252	0.6448 ± 0.0015	−330 ± 21	3525 ± 19	−328 ± 20	3196 ± 245	−21.3
	26–27	570 ± 184	0.5916 ± 0.0012	−366 ± 14	4217 ± 16	−355 ± 14	3572 ± 179	−21.3
	66–67	983 ± 139	0.5574 ± 0.0015	−372 ± 11	4695 ± 22	−354 ± 11	3588 ± 137	−21.3
	186–187	2021 ± 136	0.5154 ± 0.0014	−342 ± 11	5324 ± 22	−328 ± 11	3248 ± 135	−21.4
	248–249	2633 ± 171	0.4495 ± 0.0014	−382 ± 13	6423 ± 25	−391 ± 13	3935 ± 168	−21.5
F10B	3–4	483 ± 286	0.7093 ± 0.0015	−248 ± 26	2759 ± 17	−245 ± 26	2262 ± 279	−21.4
	28–29	1863 ± 158	0.5708 ± 0.0014	−284 ± 14	4504 ± 20	−275 ± 14	2616 ± 155	−21.0
	43–44	3171 ± 432	0.4382 ± 0.0015	−357 ± 34	6628 ± 27	−368 ± 34	3633 ± 421	−21.6
	44–52	3642 ± 467	0.4545 ± 0.0014	−294 ± 40	6334 ± 25	−313 ± 40	2944 ± 454	−21.5
	61–62	5058 ± 349	0.4208 ± 0.0010	−224 ± 33	6953 ± 19	−279 ± 33	2471 ± 340	−21.4
	78–79	6452 ± 283	0.3069 ± 0.0010	−330 ± 23	9489 ± 26	−405 ± 23	3801 ± 276	−21.7
	93–94	7431 ± 288	0.2818 ± 0.0013	−308 ± 24	10174 ± 37	−394 ± 24	3622 ± 282	−21.2
	99–106	8113 ± 76	0.2390 ± 0.0008	−362 ± 6	11498 ± 27	−432 ± 7	4154 ± 82	–22.8
	106–107	8635 ± 284	0.2912 ± 0.0009	−172 ± 29	9911 ± 25	−237 ± 29	2019 ± 277	–23.9
	109–110	9188 ± 639	0.2184 ± 0.0012	−336 ± 51	12222 ± 44	−421 ± 51	3947 ± 623	−21.9
	112–113	9696 ± 695	0.1832 ± 0.0012	−408 ± 50	13633 ± 53	−494 ± 50	4874 ± 677	–22.6
	115–116	10195 ± 801	0.1603 ± 0.0009	−450 ± 53	14706 ± 45	−576 ± 53	5755 ± 779	–23.0
	126–127	12044 ± 715	0.1331 ± 0.0008	−429 ± 50	16200 ± 48	−621 ± 50	5911 ± 696	–23.3
	136–137	13742 ± 194	0.1173 ± 0.0007	−382 ± 15	17215 ± 48	−578 ± 16	5301 ± 200	−24.0
	137–141	14103 ± 153	0.1236 ± 0.0007	−319 ± 13	16795 ± 45	−524 ± 15	4586 ± 161	−24.1

Notes: Number to right of ± is 1σ uncertainty. AIR is the apparent initial radiocarbon age. $\Delta^{14}C_{initial}$ is decay corrected radiocarbon content. $\Delta\Delta^{14}C_{org} = \Delta^{14}C_{initial} - \Delta^{14}C_{atm}$.

the period of overlap (4.6–0.5 kyr BP) average TOC values were a factor of 1.3 higher in core F11A compared to core F10B.

The crenarchaeol content of core F10B was between 25 and 1178 ng g^{-1}, displaying a gradual increase from 14.3 to 2.2 kyr BP (Fig. 3c, red) and a rapid increase from 2.0 to 0.3 kyr BP. The branched GDGT content decreased gradually from 120 ng g^{-1} at 14.3 kyr BP to 15 ng g^{-1} at 5.5 kyr BP, and then increased slightly until 0.3 kyr BP (Fig. 3d, red). In core F11A, crenarchaeol and branched GDGT contents varied between 51–1,558 ng g^{-1} and 3–56 ng g^{-1}, respectively, both showing a gradual increase from ca. 1.0 kyr BP towards present (Fig. 3c, 3d; blue). Average crenarchaeol and branched GDGT contents during the period of overlap (4.6–0.3 kyr BP) in core F11A were a factor of 1.3 and 1.1 higher, respectively, compared to core F10B.

3.2. Radiocarbon isotope and age of total organic carbon

Down-core $^{14}C_{org}$ ages (BP, relative to 1950 CE) were consistently higher than sediment ages constrained by benthic foraminiferal ^{14}C values (Fig. 2d; Table 2). In core B2B, TOC-AIR varied in a narrow range of 3200–3935 yr (Fig. 4a, green; Table 2). In core F11A, TOC-AIR varied in a relatively narrow range of 2475–3450 yr with one high value (4880 ± 120 yr) at 0.6 kyr BP (Fig. 4a, blue; Table 2). TOC-AIR in core F10B was more variable with values between 2020–5910 yr and a gradually decreasing trend since 10.1 kyr BP (Fig. 4a, red; Table 2). Relatively large uncertainties of 80–780 yr in the TOC-AIR values result from the need to interpolate between sediment age control points to determine sediment age (Fig. 4a, Table 2), since ^{14}C measurements were not performed on benthic foraminifera and TOC in the same samples.

3.3. Stable carbon isotopes of total organic carbon

TOC-$\delta^{13}C$ values in core F11A varied within a narrow range between −21.4‰ and −20.9‰, with slightly higher values over the last 1.0 kyr (Fig. 4d, blue). Five TOC-$\delta^{13}C$ values in core B2B varied within a narrow range of −21.5‰ and −21.3‰ (Fig. 4d, green). TOC-$\delta^{13}C$ values in core F10B varied in a larger range between −24.3‰ and −20.9‰ (Fig. 4d, red), with lower values of –23.3‰ to −24.3‰ from 14.0 – 10.6 kyr BP followed by a rapid increase to −21.7‰ to −20.9‰ from 7.8 – 0.5 kyr BP.

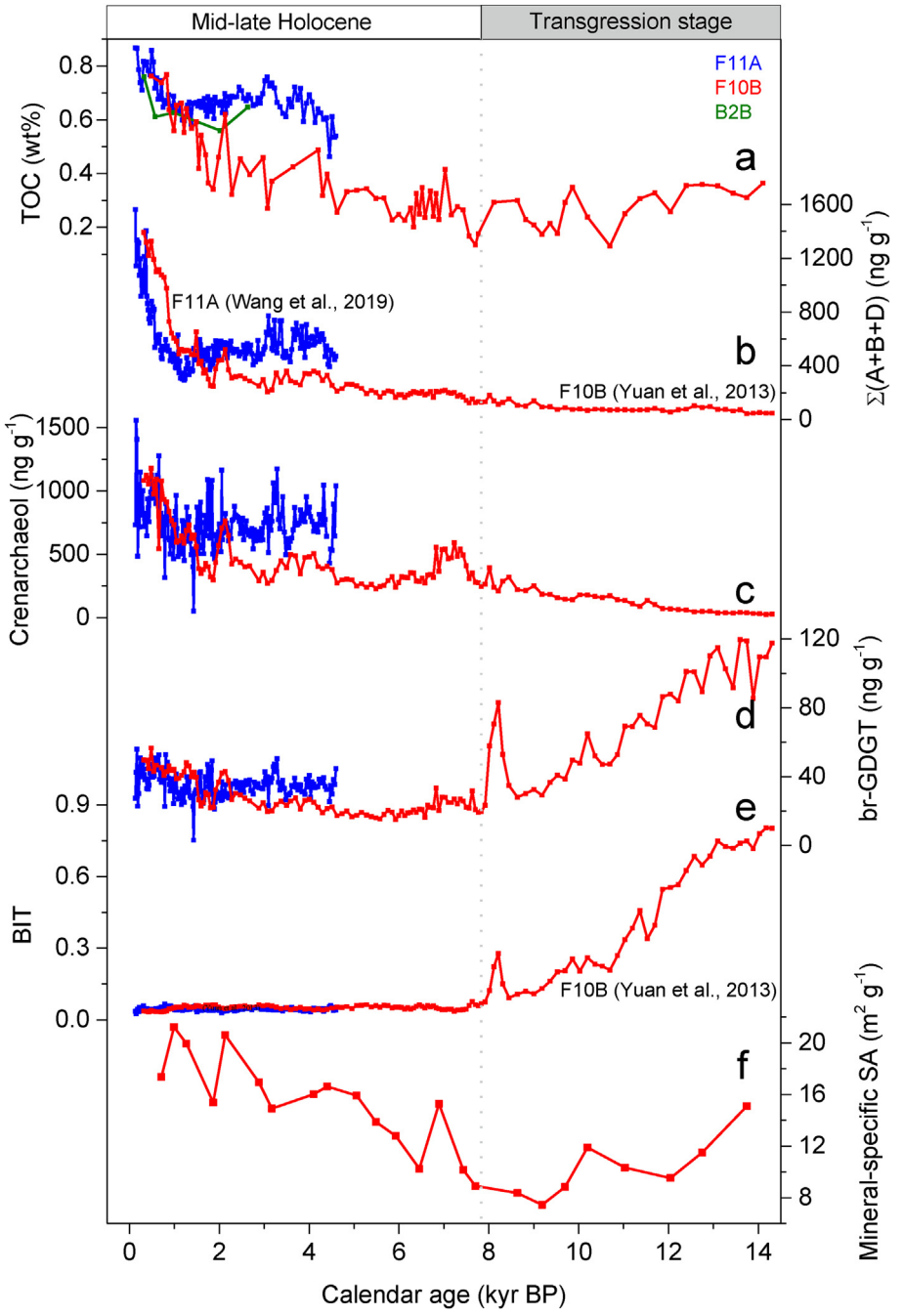

Fig. 3. Contents of TOC and biomarkers in cores F11A (in blue), B2B (in green) and F10B (in red). (a) Contents of TOC (this study). (b) Content of Σ(A + B + D), i.e., sum of C_{37} alkenones, brassicasterol and dinosterol, of core F10B (Yuan et al., 2013) and core F11A (Wang et al., 2019). (c) Contents of crenarchaeol (this study). (d) Contents of branched GDGTs (this study). (e) BIT values of cores F10B (Yuan et al., 2013) and F11A (this study). (f) Mineral-specific surface area (SA) of core F10B (this study).

During the period of overlap (4.6–0.5 kyr BP) TOC-$\delta^{13}C$ values were similar in cores F10B and F11A, except at 3.2 kyr BP and 3.6 kyr BP when values in core F10B were ~ 0.4‰ depleted relative to core F11A.

3.4. Mineral-specific SA

Mineral-specific SA varied in a range between 7.4 and 21.2 m^2 g^{-1}, displaying relatively low values of 7.4 to 15.1 m^2 g^{-1} from 13.7 – 8.6 kyr BP followed by a gradual increase to 21.2 m^2 g^{-1} at 1.0 kyr BP (Fig. 3f).

4. DISCUSSION

4.1. Rising sea levels led to organic carbon source variations

Continental shelf sediments contain a mixture of OC from terrestrial and marine sources. The slightly decreasing

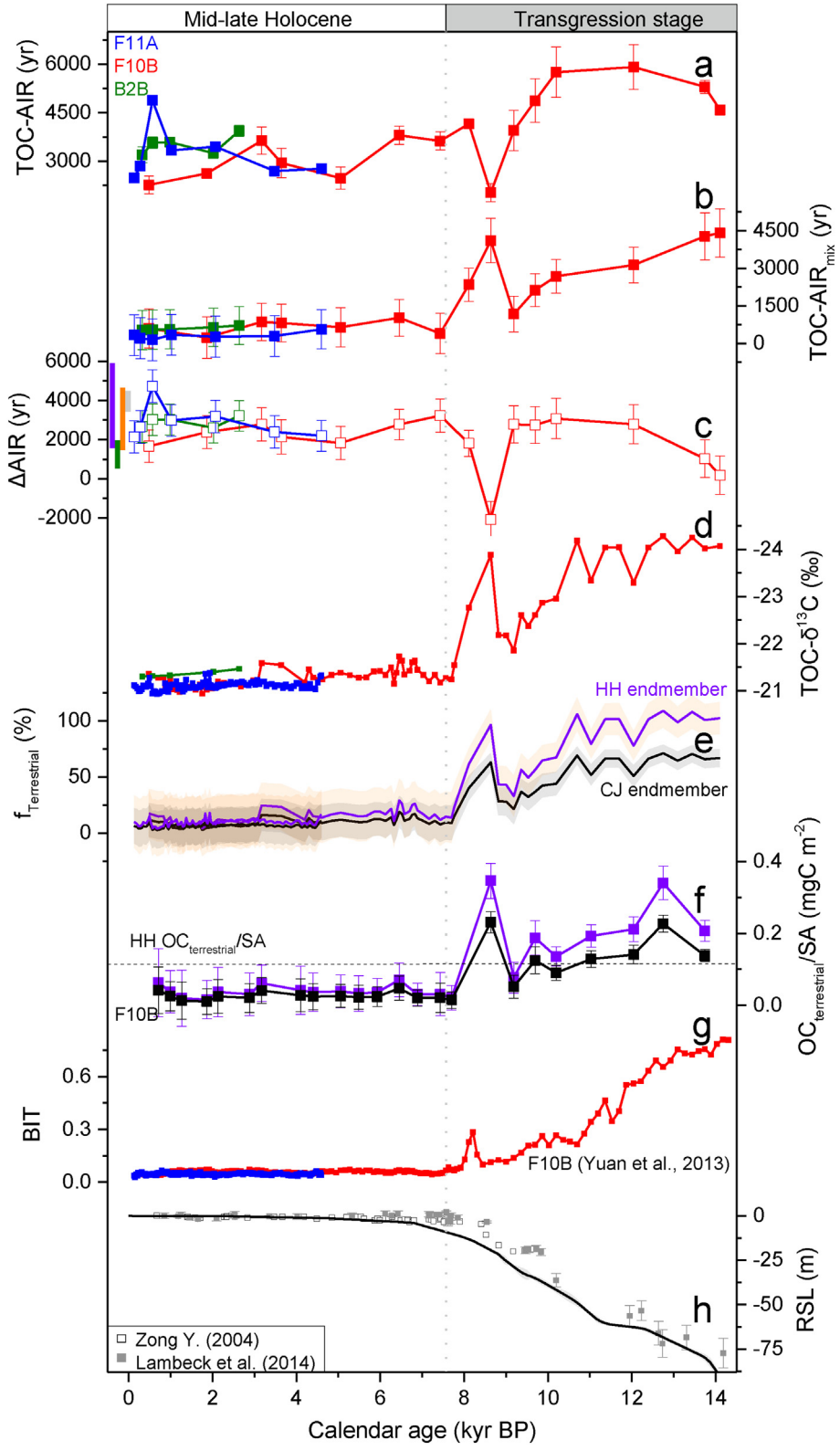
Mid-late Holocene
Transgression stage
F11A
F10B
B2B
a
b
c
d
e
f
g
h
TOC-AIR (yr)
TOC-AIR$_{mix}$ (yr)
ΔAIR (yr)
TOC-δ^{13}C (‰)
HH endmember
CJ endmember
f$_{Terrestrial}$ (%)
HH OC$_{terrestrial}$/SA
F10B
OC$_{terrestrial}$/SA (mgC m^{-2})
BIT
F10B (Yuan et al., 2013)
RSL (m)
Zong Y. (2004)
Lambeck et al. (2014)
Calendar age (kyr BP)

trend of TOC from ca. 14 to 8 kyr BP (Fig. 3a) could be attributed to a decrease of terrestrial OC input, as implied by decreasing branched GDGTs (Fig. 3d), at a time when marine OC, estimated from the sum of phytoplankton biomarkers Σ(A + B + D) (Yuan et al., 2013; Wang et al, 2019), slightly increased (Fig. 3b). Conversely, the TOC increase from ca. 7.8 to 2.1 kyr BP and from 1.3 to 0.1 kyr BP (Fig. 3a) was most likely caused by increasing marine OC input (Fig. 3b) at a time when terrestrial OC delivery was relatively constant (Fig. 3d).

More quantitative estimates of terrestrial OC delivery to the SWCIM can be made with a two-endmember mixing model using TOC-$\delta^{13}C$ values (Tao et al., 2015; Li et al., 2018; Wu et al., 2018; Yu et al., 2019). The calculations were written as follows:

$$\delta^{13}C = \delta^{13}C_{terrestrial} \times f_{terrestrial} + \delta^{13}C_{marine} \times f_{marine}, \quad (4)$$

$$f_{terrestrial} + f_{marine} = 1 \quad (5)$$

Today, the Huanghe and Changjiang provide more than 90% of the sediments to the SWCIM in the central ECS (Yuan et al., 2008; Li et al., 2012; Zhou et al., 2014; Dou et al., 2015; Yang et al., 2016; Qiao et al., 2017), and the majority of terrestrial OC in the SWCIM is similarly sourced from these two large rivers (Wu et al., 2013; Bao et al., 2018b; Jiao et al., 2018). In addition, Van der Voort et al. (2018) used a numerical clustering algorithm based on bulk OC content and $\Delta^{14}C$ to conclude that OC in SWCIM surface sediments were primarily derived from the Huanghe rather than the Changjiang or other small rivers. By the mid-late Holocene the modern current system in the Chinese marginal seas had been established (Li et al., 2014; Gao et al., 2016). Sedimentological evidence implies that Changjiang-derived sediment deposition was limited to west of 124°E (Yang et al., 2016 and references therein), and that sediment delivered to the SWCIM was mainly from the Huanghe (Yuan et al., 2008; Zhou et al., 2014; Dou et al., 2015; Yang et al., 2016). The Huanghe $\delta^{13}C_{org}$ endmember of -24.0 ± 0.4‰ was constrained by the $\delta^{13}C$ values of particulate organic carbon (POC) samples collected at the Kenli (37.68°N, 118.52°E; n = 18) hydrographic station (Fig. 1) (Tao et al., 2015; Yu et al., 2019). The Changjiang $\delta^{13}C_{org}$ endmember of -25.6 ± 0.3‰ was estimated from POC samples collected at Xuliujing (31.46°N, 120.55°E; n = 4) and Jiangyin (31.52°N, 120.32°E; n = 1) hydrographic stations (Fig. 1) (Wu et al., 2018). The marine OC endmember $\delta^{13}C$ value of -20.8 ± 0.8‰ is based on the global average for phytoplankton (Hedges et al., 1997; Blair and Aller, 2012). This value is consistent with an average $\delta^{13}C$ value of -20.9 ± 0.5‰ for marine biota in the Chinese marginal seas, including jellyfish, Labidocera, plankton and benthos (Cai, 1994), as well as with compiled marine OC-$\delta^{13}C$ endmember values of −20‰ to −21‰ in the marginal seas of China (Zhang et al., 2020). Because a two-endmember mixing model cannot be used to distinguish Huanghe and Changjiang contributions, we estimated terrestrial OC contributions ($f_{terrestrial}$) based on the extreme case of OC being sourced from each river separately. If all terrestrial OC was of Huanghe origin, the $\delta^{13}C$-based mixing model yields $f_{terrestrial}$ averaging $96.1 \pm 13.4\%$ from 14 − 10 kyr BP and $11.4 \pm 4.7\%$ during the last 7.8 kyr (Fig. 4e, purple). If all terrestrial OC was sourced from the Changjiang, the $\delta^{13}C$-based mixing model yields $f_{terrestrial}$ averaging $62.8 \pm 8.8\%$ from 14 − 10 kyr BP and $7.6 \pm 3.1\%$ during the last 7.8 kyr (Fig. 4e, black). In either case (and any intermediate circumstance) $\delta^{13}C_{org}$ values imply that sedimentary OC was mainly composed of terrestrial OC from 14 − 10 kyr BP and marine OC from 7.8 − 0.1 kyr BP.

Decreasing terrestrial OC contributions during the transgression period are supported by BIT (Branched and Isoprenoid Tetraether) index values (Fig. 3e, 4g). The BIT index has been widely used to estimate terrestrial (mostly soil) OC in marine sediments (Hopmans et al., 2004), although there are minor contributions of branched GDGTs from marine production (Zhu et al., 2011; Fietz et al., 2012). Overall, BIT index values (Fig. 4g) vary inversely with $\delta^{13}C_{org}$ values (Fig. 4d) and covary with the $f_{terrestrial}$ values (Fig. 4e) thus derived. Based on these independent methods of estimating terrestrial OC contributions to marine sediments, it is clear that terrestrial OC contributions to SWCIM sediments were highest near 14.0 kyr BP and decreased precipitously until ~9 kyr BP, with very low values since 7.8 kyr BP (Fig. 3e, 4e). The BIT and TOC-$\delta^{13}C$-derived terrestrial OC contributions in the SWCIM changed in concert with global sea level (compare Fig. 4h with Fig. 4d–g), suggesting that sea level, which dictates the distance between the coastline and our sediment core sites, is an important mechanism controlling the contribution of terrestrial OC to the SWCIM. For instance, sea level was ca. 75 m to 50 m lower than present from 14 to 11 kyr BP (Fig. 4h) during which time the coastline

Fig. 4. Comparison of paleo-records from cores B2B (in green), F10B (in red) and F11A (in blue) with sea level changes over the last 14.3 kyr. (a) Apparent initial radiocarbon age of TOC, i.e., TOC-AIR (this study). (b) Expected radiocarbon ages of OC (TOC-AIR_{mix}) based on a binary mixing model (this study). (c) ΔAIR_{OC} (difference between TOC-AIR and calculated TOC-AIR_{mix}) (this study). Purple, green, orange and grey bars in the left represent published hydrodynamic-process-induced lateral transport times of OC in the South China Sea (Wei et al., 2020), Yellow Sea (Bao et al., 2018a), ECS (Bao et al., 2019a), and the Siberian-Arctic shelf (Bröder et al., 2018), respectively. (d) TOC-$\delta^{13}C$ (this study). (e) Terrestrial OC contributions, $f_{Terrestrial}$, calculated using Huanghe (HH, purple) and Changjiang (CJ, black) $\delta^{13}C$ endmembers, respectively, and their associated 1σ uncertainty (shaded regions) (this study). (f) Normalized terrestrial OC content to mineral-specific surface area (i.e., $OC_{terrestrial}$/SA) in core F10B (this study). Terrestrial contents were calculated using $f_{terrestrial}$ derived from the Huanghe (purple) and Changjiang (black) endmembers, respectively. The dashed horizontal line represents average OC/SA in contemporary Huanghe particles (Hou et al., 2020). (g) BIT values from cores F10B (Yuan et al., 2013) and F11A (this study). (h) Rectangles represent sea level records in the Chinese marginal seas (Zong, 2004; Lambeck et al., 2014) and the black solid line represents the global sea level curve (Lambeck et al., 2014). Error bars in (a), (b), (c) and (f) correspond to propagated 1σ error based on measurement and endmember uncertainties.

was much closer to site F10B (dashed red lines in Fig. 1), providing a more direct conduit for continental OC to our core locations. By ca. 7.8 kyr BP, sea level had approached modern values (Fig. 4h), increasing the distance between the coast and our core sites (Fig. 1), and likely diminishing the flux of terrestrial OC (Fig. 5b, 5c).

4.2. Elevated $^{14}C_{org}$ ages in three cores

The ^{14}C age of TOC from the top (0–1 cm) of cores F11A and B2B were 2625 ± 20 yr and 3525 ± 20 yr, respectively (Table 2), with the former within and the latter higher than the published range of 1605 to 2755 yr (2225 ± 310 yr on average, n = 13) for surface sediments (blue dots in Fig. 1) from the SWCIM in the ECS (Bao et al., 2016). Radiocarbon ages of TOC in cores B2B, F10B and F11A exceeded atmospheric ^{14}C ages (expressed as TOC-AIR) by 2000–6000 years throughout the past 14.1 kyr, with the largest offsets occurring during the marine transgression period (Fig. 4a). This could have occurred through increased inputs of pre-aged or fossil carbon to the ECS from continents, hydrodynamic process induced OC aging within the ECS, or some combination of the two. Considering ~ 7.8 kyr BP marked the distinct temporal changes of regional sea level in China's marginal seas (Fig. 4h), the ensuing discussion of mechanisms controlling TOC-AIR variations were separated into the mid-late Holocene (ca. 7.8 to 0 kyr BP) when sea level was high and stable, and the modern tidal-current systems prevailed (Uehara and Saito, 2003), and the marine transgression stage (14.1–7.8 kyr BP) during which time the distance between the sediment core sites and the coastline gradually increased.

4.3. Processes contributing to elevated $^{14}C_{org}$ ages during the mid-late Holocene

4.3.1. Mixing of OC sources and TOC radiocarbon age variations

A plot of $\Delta^{14}C$ versus $\delta^{13}C$ (Fig. 6) can help constrain the sources of OC in the SWCIM using the contemporary endmembers because large differences exist in both the $\Delta^{14}C$ and $\delta^{13}C$ values of OC produced in situ and delivered by the two large rivers (Huanghe and Changjiang) draining into that basin (Blair et al., 2003; Tao et al., 2015; Yu et al., 2019). The parameter $\Delta\Delta^{14}C_{org}$ plotted in Fig. 6 accounts for the changing ^{14}C activity of the atmosphere ($\Delta^{14}C_{atm}$) during the last 14.1 kyr (Schefuß et al., 2016). As shown in Fig. 6, no mixing scenario between the three OC sources (Huanghe, Changjiang, and marine) can reproduce the $\Delta\Delta^{14}C_{org}$ and $\delta^{13}C$ values of TOC in cores B2B, F10B and F11A using the modern endmember values. Because the TOC-$\delta^{13}C$ values fall within the −26 to −20‰ range encompassed by the rivers and in situ (marine) production, it is the low $\Delta\Delta^{14}C_{org}$ values in the core sediments that require further explanation (Fig. 6).

One possibility is that the ^{14}C age of river-derived OC changed over time and was older throughout the mid-late Holocene than it is today. If all terrestrial OC in our sediment cores derived from the Changjiang, it would require that the majority of that OC must have been ^{14}C-dead and have had a $\delta^{13}C$ value far higher than the modern river value (Fig. 6). Because such old $^{14}C_{org}$ ages have not been observed in the lower reaches of large tropical or temperate rivers (Marwick et al., 2015 and references therein) we regard this as an unlikely possibility for the Changjiang and conclude, as prior studies do (Yuan et al., 2008; Zhou et al., 2014; Dou et al., 2015; Yang et al., 2016), that the majority of terrigenous sediment delivered to the central ECS during the mid-late Holocene was from the Huanghe. If the Huanghe supplied all of the terrestrial OC in our sediment cores, a significant proportion of that OC would have had to be ^{14}C-dead and characterized by a $\delta^{13}C$ value higher than the modern river value to account for the sediment core $\Delta^{14}C$ values (Fig. 6). Yet observations indicate that the majority (53–57%) of POC from the modern Huanghe estuary is pre-aged (Tao et al., 2015), with POC $\Delta^{14}C_{org}$ values varying from −304‰ to −451‰ (Tao et al., 2015; Yu et al., 2019) and only small spatial and temporal variations. Furthermore, the $\Delta^{14}C$ value of short-chain (C_{16}, C_{18}) fatty acids from Huanghe suspended particles, which represent the modern OC owing to their lability in the environment, was 2 ± 35‰ (Tao et al., 2016), implying that bomb-^{14}C does not bias modern riverine POC toward younger $\Delta^{14}C$ values. Taken together the evidence suggests that significant changes of Huanghe POC ^{14}C ages were unlikely during the mid-late Holocene.

Several studies have also shown that aerosols can deliver large amounts of fossil (i.e., ^{14}C-dead) OC, particularly in the form of black carbon, to the contemporary Chinese marginal seas (Fang et al., 2015; Yu et al., 2018). However, even without any contribution of pre-aged terrestrial OC, the mid-late Holocene samples would require a mixture of almost 35% fossil OC with ca. 65% of marine OC to balance the $\Delta^{14}C$ values (Fig. 6). This would be at odds with results from carbon isotope analyses on lipid biomarkers and ramped pyrolysis analyses that indicate the majority of terrestrial OC in surface sediments from the Yellow Sea and ECS is pre-aged OC derived from rivers (Tao et al., 2016; Bao et al., 2019). Furthermore, the measured $\Delta^{14}C$ values of POC in the Changjiang and Huanghe would have already incorporated the fossil carbon, making an additional contribution of this material unnecessary to produce the low $\Delta\Delta^{14}C_{org}$ values in cores B2B, F10B and F11A (Fig. 6). We thus suggest that increased fossil OC contribution was not the most important process causing $\Delta\Delta^{14}C_{org}$ that are lower than those possible from by mixing river-derived and marine OC.

4.3.2. Hydrodynamic aging of TOC

As previously proposed for surface sediments from the Chinese marginal seas (Bao et al., 2016; 2018b), we propose that the most likely mechanisms causing elevated $^{14}C_{org}$ ages of ECS sediments deposited over the last 7.8 kyr are the mixing of pre-aged terrestrial OC from the Huanghe with in situ-produced marine OC, coupled with aging during hydrodynamic processes on the shelf prior to sediment burial. Hydrodynamic process aging of OC has been demonstrated by several studies of surface sediments in the Chinese marginal seas and elsewhere (Bao et al.,

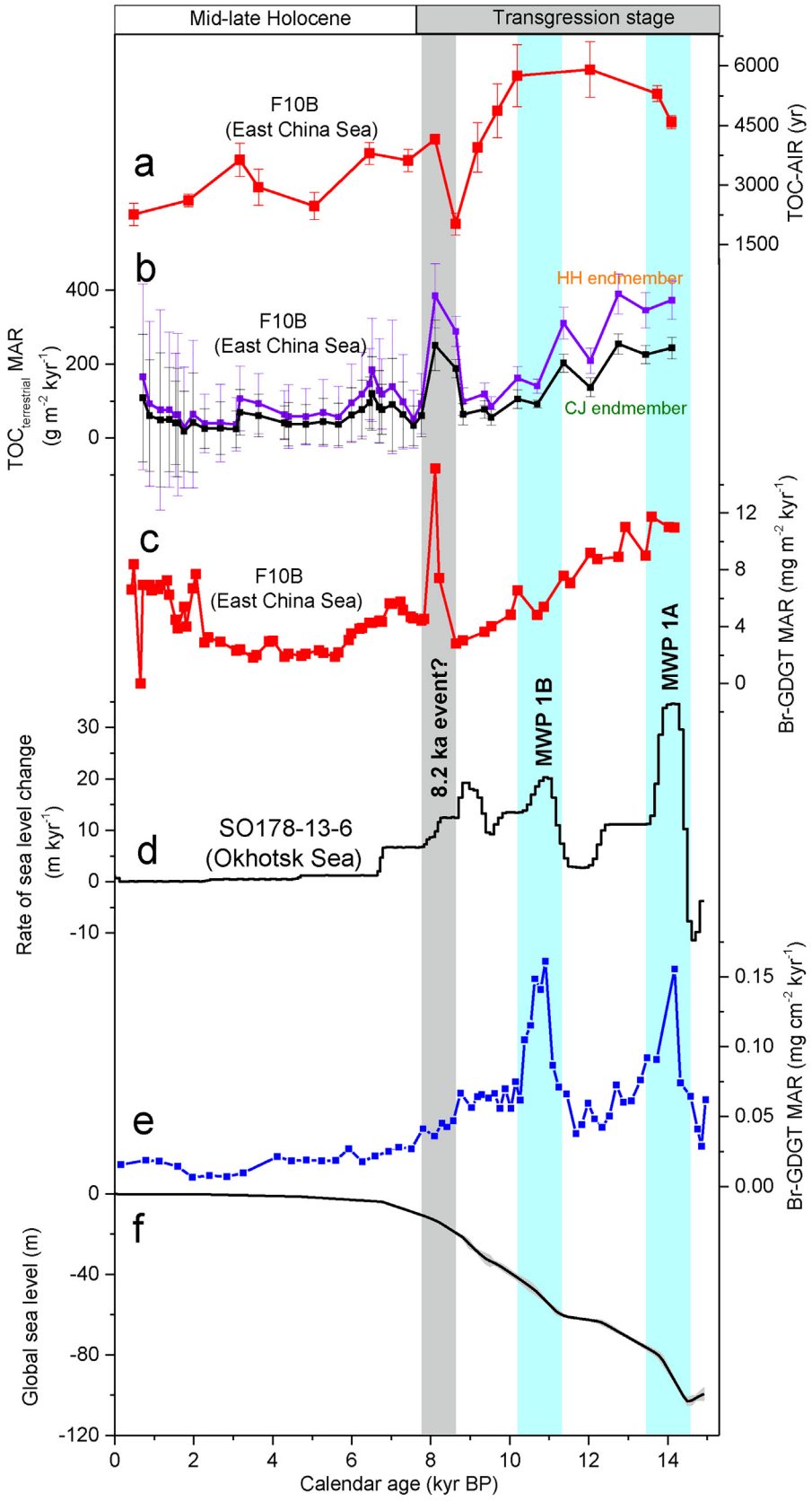

Fig. 5. Comparison of terrestrial OC records with sea level changes over the last 14.3 kyr. (a) Apparent initial radiocarbon age of TOC (i.e., TOC-AIR) in core F10B (this study). (b) Mass accumulation rate of terrestrial OC in core F10B calculated using Huanghe (HH, purple) and Changjiang (CJ, black) $\delta^{13}C$ endmembers, respectively, and their associated 1σ uncertainty (this study). (c) Mass accumulation rate of branched GDGTs in core F10B (this study). (d) Rate of global sea-level rise (Lambeck et al., 2014). (e) Mass accumulation rate of branched GDGTs in core SO178-13-6 from the Okhotsk Sea (Winterfeld et al., 2018). (f) Global sea level curve (Lambeck et al., 2014). MWP: melt water pulse.

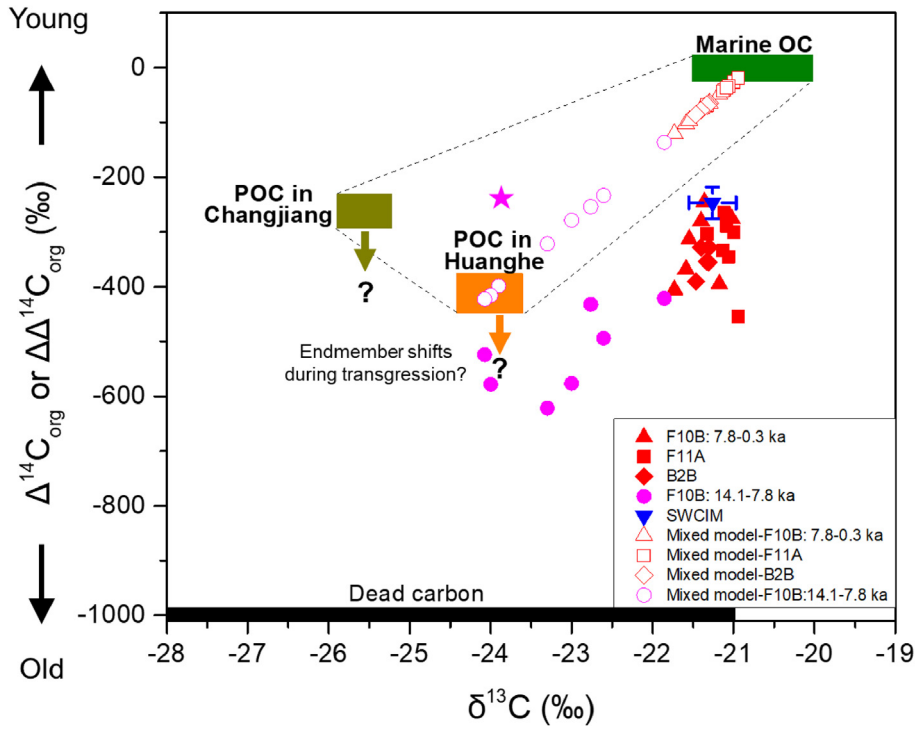

Fig. 6. Initial radiocarbon offset versus $\delta^{13}C$ of OC from marine sediments and rivers. $\Delta\Delta^{14}C_{org}$ values from cores B2B, F10B and F11A for the mid-late Holocene (7.8–0 kyr BP; red) and the transgression (14.1–7.8 kyr BP; magenta) with the data for 8.6 kyr BP labeled by a magenta star. Open symbols represent expected $\Delta\Delta^{14}C_{mix}$ values calculated using a binary mixing model based on $\delta^{13}C$ values of TOC for the three cores (see App****endix for the detailed calculation). TOC-$\Delta^{14}C_{org}$ and -$\delta^{13}C$ of surface sediments from the SWCIM (▼) are from Bao et al. (2016). Endmember values are based on the analyses of contemporary river and marine samples. POC-$\Delta^{14}C_{org}$ and -$\delta^{13}C$ endmembers of the modern Huanghe are from Tao et al. (2015) and Yu et al. (2019); POC-$\Delta^{14}C_{org}$ and -$\delta^{13}C$ endmembers of the modern Changjiang are from Wu et al. (2018). The endmembers of contemporary marine sourced OC were assumed to be $-20.8 \pm 0.8‰$ for $\delta^{13}C$ and $0 \pm 25‰$ for $\Delta^{14}C_{marine}$ (Hedges et al., 1997; Blair and Aller, 2012). Dead carbon endmember values derive from petroleum and coal (Cao et al., 2011; Gustafsson et al., 2009). Colored rectangles and error bars ($\pm 1\sigma$) represent end-member uncertainties. Error bars of core samples are not shown (see Table 2 for errors).

2018a; 2019a; Bröder et al., 2018; Mollenhauer et al., 2007). Below the extent of aging from this process in ECS cores B2B, F11A and F10B is quantified during the mid-late Holocene.

This calculation is based on the assumption discussed above that the Huanghe is the main source of terrestrial OC to the SWCIM, and the assumption that the $\delta^{13}C$ and AIR values for Huanghe POC were equivalent to the modern values of $-24.0 \pm 0.4‰$ and 4279 ± 493 yr (Tao et al., 2015; Yu et al., 2019), respectively, and constant during the mid-late Holocene. A more detailed description of these calculations is provided in the Appendix A, with a brief summary presented here. First, the marine and terrestrial proportions (f_{marine} and $f_{terrestrial}$) were calculated using the $\delta^{13}C$ mixing model (equations 4 and 5). Next, we adopt the reservoir's "relative enrichment" metric to calculate the expected radiocarbon age of OC resulting from mixing of Huanghe- and marine-derived OC (termed TOC-AIR_{mix}) constrained by the $\delta^{13}C$ binary mixing model according to the equations:

$$F^{14}R_{mix} = F^{14}R_{HH-atm} \times f_{terrestrial} + F^{14}R_{marine-atm} \times f_{marine}, \quad (6)$$

$$AIR_{mix} = -8033 \times \ln(F^{14}R_{mix}), \quad (7)$$

where $F^{14}R_{HH\text{-}atm}$ and $F^{14}R_{marine\text{-}atm}$ are enrichments of Huanghe and marine OC ^{14}C contents relative to atmospheric CO_2, respectively. In cores B2B, F10B and F11A, calculated TOC-AIR_{mix} values varied between 535–720 yr, 235–1030 yr and 150–565 yr, respectively (Fig. 4b). Averaging the three cores, calculated TOC-AIR_{mix} values during the mid-to-late Holocene were 520 ± 235 yr, which was 2650 ± 710 yr younger than the mean value of 3170 $\pm$ 670 yr for TOC-AIR. Lastly, we calculated ΔAIR_{OC} (TOC-AIR minus TOC-AIR_{mix}) to remove the influence of changing proportions of terrestrial OC on TOC-AIR ages (also see discussion in the Appendix A). For the last 7.8 kyr, ΔAIR_{OC} of three cores varied between 1580 yr and 4730 yr, averaging 2650 ± 710 yr. This average value is within the range of estimates for lateral transport times (Fig. 4c) of sediment on continental shelves due to hydrodynamic processes. Because the lateral transport time depends on the transport distance, and using the ~1400 km distance from the Huanghe estuary to the SWCIM, the averaged ΔAIR_{OC} from three cores yields a hydrodynamic-process aging of 1.9 yr km^{-1} during the mid-late Holocene. This value is comparable to the 2.0 yr km^{-1} value estimated for the pathway from the Huanghe estuary to the south Yellow Sea (Bao et al., 2018a), but lower than the 3.8–13.2 yr km^{-1} value for the pathway from the Changjiang

estuary to the Zhejiang-Fujian coast mud belt (Bao et al., 2019a) and the 6.0 yr km^{-1} value during cross-shelf transport on the Arctic continental shelf (Bröder et al., 2018).

Furthermore, even if the Huanghe POC AIR endmember varied in a larger range during the mid-late Holocene, it only changes the ΔAIR_{OC} values but not our conclusions. For example, if we consider Huanghe POC AIR values of 10,000 yr and 1000 yr, respectively, the calculated ΔAIR_{OC} values are in the ranges of 1195–4620 yr (2310 ± 755 yr on average) and 2095–4835 yr (3085 ± 640 yr on average), respectively, during the mid-late Holocene. This provides further support that potential deviations of the terrestrial OC ^{14}C endmember from the modern value cannot fully explain the TOC-AIR values during the mid-late Holocene.

Hydrodynamic processes contributing to the aging of OC in the Chinese marginal seas include tidal-current induced resuspension and offshore lateral transport of sediments (Bian et al., 2013; Bao et al., 2019a; 2019b). During cross-shelf transport selective degradation of younger terrestrial and marine OC in repeated deposition-resuspension loops causes lower terrestrial OC loading (normalized terrestrial OC contents to mineral-specific surface area, i.e., $OC_{terrestrial}/SA$) and elevated radiocarbon ages in the residual OC buried in SWCIM sediments (Bao et al., 2018b; 2019a; 2019b). This is supported by the low $OC_{terrestrial}/SA$ values of 0.02–0.07 mgC m^{-2} in core F10B during the mid-late Holocene compared with modern Huanghe particle OC/SA values of 0.09–0.25 mgC m^{-2} at Kenli hydrographic station (Fig. 4f) (Yu et al., 2019; Hou et al., 2020), which reflects substantial terrestrial OC degradation during the lateral transport from the Huanghe estuary to SWCIM. Additionally, terrestrial OC is more resistant to degradation than marine OC and its apparent lateral transport time may approach several millennia from river mouth to offshore depocenter (Bao et al., 2018a; Bröder et al., 2018; Wei et al., 2020).

In addition, TOC-AIR values are 955–1070 yr higher in cores B2B and F11A than in core F10B during the interval of overlap (2.6–0.1 kyr BP; Fig. 4a), with smaller differences in ΔAIROC values (Fig. 4c). Uncertainties with interpolated sediment ages (Table 2) might partially contribute to this discrepancy (see Appendix A). Another possible cause for these age differences is the effect of sediment grain size on OC preservation during lateral transport of sediment. As reported by Bao et al. (2018b), smaller sediment grain sizes are observed in the central part of the SWCIM than in the surrounding regions. Finer grain sizes provide more surface area for OC adsorption, and result in greater OC preservation during lateral transport (Bao et al., 2018a; 2019a). This could account for less OC aging in core F10B, in the central SWCIM, than in cores B2B and F11A on the periphery of the SWCIM.

4.4. Processes contributing to elevated $^{14}C_{org}$ ages during the marine transgression

During the transgression stage the average TOC-AIR was 4930 ± 760 yr (excluding the data from 8.6 kyr BP, as discussed below), ~2000 yr higher than the average TOC-AIR for the mid-late Holocene. However, potential factors affecting marine sediment $^{14}C_{org}$ during the transgression stage might be more complicated than in the mid-late Holocene, as both the sources (and endmember $^{14}C_{org}$ values) of terrestrial OC transported to the SWCIM and the intensity of hydrodynamic processing might have changed significantly in response to rapid sea-level-rise and coastal-current system changes (Uehara and Saito, 2003; Lambeck et al., 2014).

The mixing of different proportions of pre-aged terrestrial OC and contemporary marine OC has the potential to cause older TOC ages during the transgression stage since variations of TOC-AIR (Fig. 4a) track changes in $f_{terrestrial}$ (Fig. 4e) and BIT (Fig. 4g) records. However, from 14.1 – 9.7 kyr BP, TOC-AIR was older than endmember ages of POC from the modern Huanghe and Changjiang, requiring a substantially older terrestrial OC endmember to satisfy a terrestrial-marine mixing scenario.

Sources and ages of river POC could have changed considering the hydrologic changes that occurred in the Huanghe and Changjiang drainage basins (Wang et al., 2008; Chen et al., 2019). Previous studies indicated that soil carbon residence times increased significantly on glacial/deglacial timescales during cooler and drier periods, supplying older terrestrial OC to continental margins (Hein et al., 2020; Martens et al., 2020). However, even without any contribution of pre-aged terrestrial OC, the transgression-age samples would require a mixture of almost 50% fossil OC with ca. 50% of marine OC to balance the $\Delta^{14}C$ values (Fig. 6). It thus seems unlikely that enough ^{14}C-dead OC could have been supplied by the Haunghe or Changjiang in tropical and temperate regions (Tao et al., 2015; Wu et al., 2018; Marwick et al., 2015, and references therein).

Another potential source of pre-aged OC is eroded sediments from old delta or tidal-flat areas as sea level rose and flooded the coastline (Gao et al., 2016). Under the influence of strong tidal-currents (Uehara and Saito, 2003), newly submerged paleo-coastal regions might have served as significant sources of older OC (Kao et al., 2008). As shown in Fig. 5, both higher TOC-AIR and higher accumulation rates of $OC_{terrestrial}$ and soil microbial branched GDGTs characterized the transgression period. A recent study using dolomite/calcite ratios and rare earth elements showed that sediment in the SWCIM primarily consists of reworked sediments from the submerged East China Sea shelf during the transgression stage (Hu et al., 2014), providing further support for paleo-coastal erosion supplying old carbon.

On the Siberian-Arctic continental margin as well as in the Bering Sea, the Okhotsk Sea and the Northwest Pacific, flooding-induced erosion of old carbon from permafrost regions during melt water pulses (MWP) has been proposed as the primary process supplying strongly pre-aged sediments during the transgression stage (Fig. 5d, 5e) (Keskitalo et al., 2017; Winterfeld et al., 2018; Meyer et al., 2019; Martens et al., 2020). Yet at our site accumulation rates of $OC_{terrestrial}$ and soil microbial branched GDGTs decreased gradually from high values near 13.5 kyr BP towards the mid-late Holocene with a distinct peak near 8.0–8.6 kyr BP, and reached constant low values after 7.8 kyr BP (Fig. 5b, 5c). Within age uncertainty, pronounced peaks of accumulation rates in terrestrial OC dur-

ing the MWP events centered at ~ 14 and ~ 11 kyr BP are not observed in core F10B. This difference between high- and mid-latitude regions might reflect distinct differences in coastal erosion processes. For example, Arctic permafrost mobilization is sensitive to climate warming that co-occurred with MWP events (Keskitalo et al., 2017; Winterfeld et al., 2018; Meyer et al., 2019; Martens et al., 2020), while coastal erosion in the ECS might be more sensitive to sea level rise due to the widespread existence of strong tidal-current throughout the transgression stage (Uehara and Saito, 2003).

An anomalous low TOC-AIR value of 2020 ± 280 yr occurred at 8.6 kyr BP (Fig. 4a). Using the same calculation as in Section 4.3.2, the ΔAIR_{OC} would be −1750 ± 485 yr. Taken together with synchronous higher values of $OC_{terrestrial}$ mass accumulation rate (Fig. 5b, 5c) and $OC_{terrestrial}$/SA (Fig. 4f), this implies a sudden deposition of terrestrial OC that is younger than the modern Huanghe endmember value (Fig. 6). With a single data point any association with global or regional climate events is tentative, but the timing of this anomalous ΔAIR_{OC} value matches that of the global "8.2 ka Event" (Rohling and Pälike, 2005) within age uncertainty. A sudden and short-lived change in organic carbon cycling in eastern China and the Chinese marginal seas could have been caused by changes in the East Asian Monsoon and associated alterations of vegetation cover, river discharge, and sediment transport (Wang et al., 2005; Jia et al., 2019). Additional $\Delta^{14}C_{org}$ and $\delta^{13}C_{org}$ measurements during the 8–9 kyr BP time period in adjacent sediment cores are needed to verify this association.

Lastly, $OC_{terrestrial}$ loading ($OC_{terrestrial}$/SA) decreased gradually as sea level rose from ~ 13 kyr BP to ~ 9 kyr BP (Fig. 4f), indicating lower terrestrial OC burial efficiencies. A possible explanation for this trend is the increasing transport distance between the coastline (or river mouths) and the sediment depocenter as sea level rose, which can increase the number of deposition-resuspension loops. This provides evidence that hydrodynamic process aging might also play a role in shaping the TOC-AIR during transgression. Future studies should focus on better constraining the variations of river and eroded sediment endmembers with $\delta^{13}C$ and $\Delta^{14}C$ analyses on specific biomarkers, such as long-chain fatty acids for terrestrial OC and dinosterol or alkenones for marine OC. This will help to distinguish processes contributing to elevated $^{14}C_{org}$ ages during the marine transgression stage.

5. CONCLUSIONS

The ^{14}C and ^{13}C content of organic carbon and the lipid biomarker composition of sediments from the SWCIM in the ECS were measured to determine the sources and processes contributing to OC ages during the last 14.3 kyr, and how these changed as sea level rose by ~75 m, greatly expanding the size of the Chinese marginal seas.

OC radiocarbon ages in the SWCIM were persistently 1930–5530 yr older than co-deposited sediment ages, averaging 4415 ± 1190 yr older during the transgression 14.1–7.8 kyr BP, and 2995 ± 555 yr older since 7.8 kyr BP. These old ages of OC are attributed to the addition of pre-aged and fossil carbon from land (primarily via the Huanghe) and the hydrodynamic processing of sediment prior to burial. It is hypothesized that greater transport distances between river mouths and sediment depocenters since the current sea-level high stand began at 7.8 kyr BP and allowed for additional deposition-resuspension loops beyond what occurred when sea level was ~75 m lower than today at 14 kyr BP. Therefore, hydrodynamic process aging was the primary cause of apparent OC aging during the mid-late Holocene. During the marine transgression stage, coastal erosion may act as an important process to provide larger amounts of older carbon than during the mid-late Holocene. In addition, hydrodynamic processing aging may also shape the temporal variation of apparent OC ^{14}C ages.

These results offer new insights on the processes controlling OC ages and burial in shallow marginal seas. Anthropogenic and natural changes in the delivery of terrestrial OC to marginal seas from river discharge management, climate, land use changes, fish trawling, and other processes have the potential to fundamentally alter OC cycling and burial in marginal seas, and these impacts can be evaluated using the coupled ^{14}C, ^{13}C, and biomarker approach presented here.

Declaration of Competing Interest

The author declare that there is no conflict of interest.

ACKNOWLEDGMENTS

We sincerely appreciate of the time and effort provided by two anonymous reviewers to improve this paper. The study was supported by the National Key Research and Development Program of China (Grant No. 2016YFA0601403), the National Natural Science Foundation of China (Grant Nos. 41876076 and 91958104) and the Fundamental Research Funds for the Central Universities (Grant Nos. 202041007 and 201813029). This is MCTL (Key Laboratory of Marine Chemistry Theory and Technology) contribution #217.

APPENDIX A. SUPPLEMENTARY MATERIAL

Supplementary data to this article can be found online at https://doi.org/10.1016/j.gca.2021.04.015.

REFERENCES

Alexander C. R., DeMaster D. J. and Nittrouer C. A. (1991) Sediment accumulation in a modern epicontinental-shelf setting: The Yellow Sea. *Mar. Geol.* **98**, 51–72.

Ausín B., Magill C., Haghipour N., Fernández Á., Wacker L., Hodell D., Baumann K.-H. and Eglinton T. I. (2019) (In)coherent multiproxy signals in marine sediments: Implications for high-resolution paleoclimate reconstruction. *Earth Planet. Sci. Lett.* **515**, 38–46.

Bao R., McIntyre C., Zhao M., Zhu C., Kao S.-J. and Eglinton T. I. (2016) Widespread dispersal and aging of organic carbon in shallow marginal seas. *Geology* **44**, 791–794.

Bao R., Uchida M., Zhao M., Haghipour N., Montlucon D., McNichol A., Wacker L., Hayes J. M. and Eglinton T. I. (2018a) Organic carbon aging during across-shelf transport. *Geophys. Res. Lett.* **45**, 8425–8434.

Bao R., van der Voort T. S., Zhao M., Guo X., Montluçon D. B., McIntyre C. and Eglinton T. I. (2018b) Influence of hydrodynamic processes on the fate of sedimentary organic matter on continental margins. *Glob. Biogeochem. Cycles* **32**, 1420–1432.

Bao R., Zhao M., McNichol A., Galy V., McIntyre C., Haghipour N. and Eglinton T. I. (2019a) Temporal constraints on lateral organic matter transport along a coastal mud belt. *Org. Geochem.* **128**, 86–93.

Bao R., Zhao M., McNichol A., Wu Y., Guo X., Haghipour N. and Eglinton T. I. (2019b) On the origin of aged sedimentary organic matter along a river-shelf-deep ocean transect. *J. Geophys. Res.-Biogeosci.* **124**, 2582–2594.

Bian C., Jiang W. and Greatbatch R. J. (2013) An exploratory model study of sediment transport sources and deposits in the Bohai Sea, Yellow Sea, and East China Sea. *J. Geophys. Res.-Oceans* **118**, 5908–5923.

Blaauw M. and Christen J. A. (2011) Flexible paleoclimate age-depth models using an autoregressive gamma process. *Bayesian Anal.* **6**, 457–474.

Blair N. E. and Aller R. C. (2012) The fate of terrestrial organic carbon in the marine environment. *Annu. Rev. Mar. Sci.* **4**, 401–423.

Blair N. E., Leithold E. L., Ford S. T., Peeler K. A., Holmes J. C. and Perkey D. W. (2003) The persistence of memory: the fate of ancient sedimentary organic carbon in a modern sedimentary system. *Geochim. Cosmochim. Acta* **67**, 63–73.

Bröder L., Tesi T., Andersson A., Semiletov I. and Gustafsson Ö. (2018) Bounding cross-shelf transport time and degradation in Siberian-Arctic land-ocean carbon transfer. *Nat. Commun.* **9**, 806.

Burdige D. J. (2005) Burial of terrestrial organic matter in marine sediments: a re-assessment. *Glob. Biogeochem. Cycles* **19**, GB4011.

Cai D.-L. (1994) Geochemical Studies on Organic Carbon Isotope of the Huanghe River(Yellow River) Estuary. *Sci. China Ser. B* **37**, 1001–1015.

Cao J. J., Chow J. C., Tao J., Lee S. C., Watson J. G., Ho K. F., Wang G. H., Zhu C. S. and Han Y. M. (2011) Stable carbon isotopes in aerosols from Chinese cities: influence of fossil fuels. *Atmos. Environ.* **45**, 1359–1363.

Cartapanis O., Bianchi D., Jaccard S. L. and Galbraith E. D. (2016) Global pulses of organic carbon burial in deep-sea sediments during glacial maxima. *Nat. Commun.* **7**, 10796.

Chen F., Chen J., Huang W., Chen S., Huang X., Jin L., Jia J., Zhang X., An C., Zhang J., Zhao Y., Yu Z., Zhang R., Liu J., Zhou A. and Feng S. (2019) Westerlies Asia and monsoonal Asia: Spatiotemporal differences in climate change and possible mechanisms on decadal to sub-orbital timescales. *Earth-Sci. Rev.* **192**, 337–354.

DeMaster D. J., McKee B. A., Nittrouer C. A., Jiangchu Q. and Guodong C. (1985) Rates of sediment accumulation and particle reworking based on radiochemical measurements from continental shelf deposits in the East China Sea. *Cont. Shelf Res.* **4**, 143–158.

Dou Y., Yang S., Lim D.-I. and Jung H.-S. (2015) Provenance discrimination of last deglacial and Holocene sediments in the southwest of Cheju Island, East China Sea. *Palaeogeogr. Palaeoclimatol. Palaeoecol.* **422**, 25–35.

Drenzek N. J., Hughen K. A., Montluçon D. B., Southon J. R., dos Santos G. M., Druffel E. R. M., Giosan L. and Eglinton T. I. (2009) A new look at old carbon in active margin sediments. *Geology* **37**, 239–242.

Fang Y., Chen Y., Tian C., Lin T., Hu L., Huang G., Tang J., Li J. and Zhang G. (2015) Flux and budget of BC in the continental shelf seas adjacent to Chinese high BC emission source regions. *Glob. Biogeochem. Cycles* **29**, 957–972.

Fietz S., Huguet C., Bendle J., Escala M., Gallacher C., Herfort L., Jamieson R., Martínez-Garcia A., McClymont E. L., Peck V. L., Prahl F. G., Rossi S., Rueda G., Sanson-Barrera A. and Rosell-Melé A. (2012) Co-variation of crenarchaeol and branched GDGTs in globally-distributed marine and freshwater sedimentary archives. *Global Planet. Change* **92–93**, 275–285.

Galy V., Beyssac O., France-Lanord C. and Eglinton T. (2008) Recycling of Graphite During Himalayan Erosion: A Geological Stabilization of Carbon in the Crust. *Science* **322**, 943–945.

Gao S., Wang D., Yang Y., Zhou L., Zhao Y., Gao W., Han Z., Yu Q. and Li G. (2016) Holocene sedimentary systems on a broad continental shelf with abundant river input: process–product relationships. *Geol. Society London, Spec. Publ.* **429**, 223–259.

Griffith D. R., Martin W. R. and Eglinton T. I. (2010) The radiocarbon age of organic carbon in marine surface sediments. *Geochim. Cosmochim. Acta.* **74**, 6788–6800.

Gustafsson Ö., Kruså M., Zencak Z., Sheesley R. J., Granat L., Engström E., Praveen P., Rao P., Leck C. and Rodhe H. (2009) Brown clouds over South Asia: biomass or fossil fuel combustion? *Science* **323**, 495–498.

Hedges J. I., Keil R. G. and Benner R. (1997) What happens to terrestrial organic matter in the ocean? *Org. Geochem.* **27**, 195–212.

Hein C. J., Usman M., Eglinton T. I., Haghipour N. and Galy V. V. (2020) Millennial-scale hydroclimate control of tropical soil carbon storage. *Nature* **581**, 63–66.

Honda M. C., Kusakabe M., Nakabayashi S. and Katagiri M. (2000) Radiocarbon of sediment trap samples from the Okinawa trough: lateral transport of ^{14}C-poor sediment from the continental slope. *Mar. Chem.* **68**, 231–247.

Hopmans E. C., Weijers J. W. H., Schefuß E., Herfort L., Sinninghe Damsté J. S. and Schouten S. (2004) A novel proxy for terrestrial organic matter in sediments based on branched and isoprenoid tetraether lipids. *Earth Planet. Sci. Lett.* **224**, 107–116.

Hou P., Yu M., Zhao M., Montluçon D. B., Su C. and Eglinton T. I. (2020) Terrestrial Biomolecular Burial Efficiencies on Continental Margins. *J. Geophys. Res.-Biogeosci.* **125**, e2019JG005520.

Hu B., Yang Z., Qiao S., Zhao M., Fan D., Wang H., Bi N. and Li J. (2014) Holocene shifts in riverine fine-grained sediment supply to the East China Sea Distal Mud in response to climate change. *Holocene* **24**, 1253–1268.

Jia Y., Li D.-W., Yu M., Zhao X., Xiang R., Li G., Zhang H. and Zhao M. (2019) High- and low-latitude forcing on the south Yellow Sea surface water temperature variations during the Holocene. *Global Planet. Change* **182** 103025.

Jiao N., Liang Y., Zhang Y., Liu J., Zhang Y., Zhang R., Zhao M., Dai M., Zhai W., Gao K., Song J., Yuan D., Li C., Lin G., Huang X., Yan H., Hu L., Zhang Z., Wang L., Cao C., Luo Y., Luo T., Wang N., Dang H., Wang D. and Zhang S. (2018) Carbon pools and fluxes in the China Seas and adjacent oceans. *Sci. China-Earth Sci.* **61**, 1535–1563.

Kao S. J., Dai M. H., Wei K. Y., Blair N. E. and Lyons W. B. (2008) Enhanced supply of fossil organic carbon to the Okinawa Trough since the last deglaciation. *Paleoceanography* **23**, PA2207.

Keskitalo K., Tesi T., Bröder L., Andersson A., Pearce C., Sköld M., Semiletov I. P., Dudarev O. V. and Gustafsson Ö. (2017) Sources and characteristics of terrestrial carbon in Holocene-

scale sediments of the East Siberian Sea. *Clim. Past* **13**, 1213–1226.

Kim S.-Y. and Lim D.-I. (2014) Signatures of the late Holocene Neoglacial cold event and their marine–terrestrial linkage in the northwestern Pacific margin. *Prog. Oceanogr.* **124**, 54–65.

Lambeck K., Rouby H., Purcell A., Sun Y. and Sambridge M. (2014) Sea level and global ice volumes from the Last Glacial Maximum to the Holocene. *Proc. Natl. Acad. Sci.* **111**, 15296–15303.

Leithold E. L., Blair N. E., Childress L. B., Brulet B. R., Marden M., Orpin A. R., Kuehl S. A. and Alexander C. R. (2013) Signals of watershed change preserved in organic carbon buried on the continental margin seaward of the Waipaoa River. *New Zealand. Mar. Geol.* **346**, 355–365.

Leithold E. L., Blair N. E. and Wegmann K. W. (2016) Source-to-sink sedimentary systems and global carbon burial: a river runs through it. *Earth-Sci. Rev.* **153**, 30–42.

Li D., Zhao M., Tian J. and Li L. (2013) Comparison and implication of TEX_{86} and $U^{K'}_{37}$ temperature records over the last 356 kyr of ODP Site 1147 from the northern South China Sea. *Palaeogeogr. Palaeoclimatol. Palaeoecol.* **376**, 213–223.

Li D.-W., Chang Y.-P., Li Q., Zheng L., Ding X. and Kao S.-J. (2018) Effect of sea-level on organic carbon preservation in the Okinawa Trough over the last 91 kyr. *Mar. Geol.* **399**, 148–157.

Li G., Li P., Liu Y., Qiao L., Ma Y., Xu J. and Yang Z. (2014) Sedimentary system response to the global sea level change in the East China Seas since the last glacial maximum. *Earth-Sci. Rev.* **139**, 390–405.

Li J., Hu B., Dou Y., Zhao J. and Li G. (2012) Modern Sedimentation Rate, Budget and Supply of the Muddy Deposits in the East China Seas. *Geol. Rev.* **58**, 745–756 (in Chinese with English abstract).

Liu J., Zhu R. and Li G. (2003) Rock magnetic properties of the fine-grained sediment on the outer shelf of the East China Sea: implication for provenance. *Mar. Geol.* **193**, 195–206.

Marwick T. R., Tamooh F., Teodoru C. R., Borges A. V., Darchambeau F. and Bouillon S. (2015) The age of river-transported carbon: A global perspective. *Glob. Biogeochem. Cycles* **29**, 122–137.

Martens J., Wild B., Muschitiello F., O'Regan M., Jakobsson M., Semiletov I., Dudarev O. V. and Gustafsson Ö. (2020) Remobilization of dormant carbon from Siberian-Arctic permafrost during three past warming events. *Sci. Adv.* **6**, eabb6546.

Mayer L. M. (1994) Surface area control of organic carbon accumulation in continental shelf sediments. *Geochim. Cosmochim. Acta* **58**, 1271–1284.

McNichol A. P., Jones G. A., Hutton D. L., Gagnon A. R. and Key R. M. (1994) The rapid preparation of seawater ΣCO_2 for radiocarbon analysis at the national ocean sciences ams facility. *Radiocarbon* **36**, 237–246.

Meyer V. D., Hefter J., Köhler P., Tiedemann R., Gersonde R., Wacker L. and Mollenhauer G. (2019) Permafrost-carbon mobilization in Beringia caused by deglacial meltwater runoff, sea-level rise and warming. *Environ. Res. Lett.* **14** 085003.

Milliman J. D., Beardsley R. C., Yang Z. and Limeburner R. (1985) Modern Huanghe-derived muds on the outer shelf of the East China Sea: identification and potential transport mechanisms. *Cont. Shelf Res.* **4**, 175–188.

Mollenhauer G., Kienast M., Lamy F., Meggers H., Schneider R. R., Hayes J. M. and Eglinton T. I. (2005) An evaluation of ^{14}C age relationships between co-occurring foraminifera, alkenones, and total organic carbon in continental margin sediments. *Paleoceanography* **20**, PA1016.

Mollenhauer G., Inthorn M., Vogt T., Zabel M., Sinninghe Damsté J. S. and Eglinton T. I. (2007) Aging of marine organic matter during cross-shelf lateral transport in the Benguela upwelling system revealed by compound-specific radiocarbon dating, *Geochem. Geophys. Geosyst.* **8**, Q09004.

Ohkouchi N., Eglinton T. I., Keigwin L. D. and Hayes J. M. (2002) Spatial and Temporal Offsets Between Proxy Records in a Sediment Drift. *Science* **298**, 1224–1227.

Pearson A., McNichol A. P., Schneider R. J., Von Reden K. F. and Zheng Y. (1997) Microscale AMS ^{14}C Measurement at NOSAMS. *Radiocarbon* **40**, 61–75.

Qiao S., Shi X., Wang G., Zhou L., Hu B., Hu L., Yang G., Liu Y., Yao Z. and Liu S. (2017) Sediment accumulation and budget in the Bohai Sea, Yellow Sea and East China Sea. *Mar. Geol.* **390**, 270–281.

Reimer P. J., Bard E., Bayliss A., Beck J. W., Blackwell P. G., Ramsey C. B., Buck C. E., Cheng H., Edwards R. L. and Friedrich M. (2013) IntCal13 and Marine13 radiocarbon age calibration curves 0–50,000 years cal BP. *Radiocarbon* **55**, 1869–1887.

Rohling E. J. and Pälike H. (2005) Centennial-scale climate cooling with a sudden cold event around 8,200 years ago. *Nature* **434**, 975–979.

Schefuß E., Eglinton T. I., Spencer-Jones C. L., Rullkötter J., De Pol-Holz R., Talbot H. M., Grootes P. M. and Schneider R. R. (2016) Hydrologic control of carbon cycling and aged carbon discharge in the Congo River basin. *Nat. Geosci.* **9**, 687–690.

Sigman D. M. and Boyle E. A. (2000) Glacial/interglacial variations in atmospheric carbon dioxide. *Nature* **407**, 859–869.

Tao S., Eglinton T. I., Montluçon D. B., McIntyre C. and Zhao M. (2015) Pre-aged soil organic carbon as a major component of the Yellow River suspended load: Regional significance and global relevance. *Earth Planet. Sci. Lett.* **414**, 77–86.

Tao S., Eglinton T. I., Montluçon D. B., McIntyre C. and Zhao M. (2016) Diverse origins and pre-depositional histories of organic matter in contemporary Chinese marginal sea sediments. *Geochim. Cosmochim. Acta* **191**, 70–88.

Uehara K. and Saito Y. (2003) Late Quaternary evolution of the Yellow/East China Sea tidal regime and its impacts on sediments dispersal and seafloor morphology. *Sediment. Geol.* **162**, 25–38.

Van der Voort T. S., Mannu U., Blattmann T. M., Bao R., Zhao M. and Eglinton T. I. (2018) Deconvolving the Fate of Carbon in Coastal Sediments. *Geophys. Res. Lett.* **45**, 4134–4142.

Wang Y., Cheng H., Edwards R. L., He Y., Kong X., An Z., Wu J., Kelly M. J., Dykoski C. A. and Li X. (2005) The Holocene Asian monsoon: links to solar changes and North Atlantic climate. *Science* **308**, 854–857.

Wang Y., Cheng H., Edwards R. L., Kong X., Shao X., Chen S., Wu J., Jiang X., Wang X. and An Z. (2008) Millennial- and orbital-scale changes in the East Asian monsoon over the past 224,000 years. *Nature* **451**, 1090–1093.

Wang Z., Xiao X., Yuan Z., Wang F., Xing L., Gong X., Kubota Y., Uchida M. and Zhao M. (2019) Air-sea interactive forcing on phytoplankton productivity and community structure changes in the East China Sea during the Holocene. *Global Planet. Change* **179**, 80–91.

Wei B., Mollenhauer G., Hefter J., Grotheer H. and Jia G. (2020) Dispersal and aging of terrigenous organic matter in the Pearl River Estuary and the northern South China Sea Shelf. *Geochim. Cosmochim. Acta* **282**, 324–339.

Winterfeld M., Mollenhauer G., Dummann W., Köhler P., Lembke-Jene L., Meyer V. D., Hefter J., McIntyre C., Wacker L., Kokfelt U. and Tiedemann R. (2018) Deglacial mobilization of pre-aged terrestrial carbon from degrading permafrost. *Nat. Commun.* **9**, 3666.

Wu Y., Eglinton T., Yang L., Deng B., Montluçon D. and Zhang J. (2013) Spatial variability in the abundance, composition, and

age of organic matter in surficial sediments of the East China Sea. *J. Geophys. Res.-Biogeosci.* **118**, 1495–1507.

Wu Y., Eglinton T. I., Zhang J. and Montlucon D. B. (2018) Spatiotemporal variation of the quality, origin, and age of particulate organic matter transported by the Yangtze River (Changjiang). *J. Geophys. Res.-Biogeosci.* **123**, 2908–2921.

Xing L., Jiang Y., Yuan Z., Zhang H., Li L., Zhou L. and Zhao M. (2013) Holocene temperature records from the East China sea mud area southwest of the Cheju Island reconstructed by the $U^{K'}_{37}$ and TEX_{86} paleothermometers. *J. Ocean Univ.* **12**, 599–604.

Yang S., Bi L., Li C., Wang Z. and Dou Y. (2016) Major sinks of the Changjiang (Yangtze River)-derived sediments in the East China Sea during the late Quaternary. *Geol. Soc. Lond. Special Publ.* **429**, 137–152.

Yu M., Guo Z., Wang X., Eglinton T. I., Yuan Z., Xing L., Zhang H. and Zhao M. (2018) Sources and radiocarbon ages of aerosol organic carbon along the east coast of China and implications for atmospheric fossil carbon contributions to China marginal seas. *Sci. Total Environ.* **619–620**, 957–965.

Yu M., Eglinton T. I., Haghipour N., Montluçon D. B., Wacker L., Hou P., Zhang H. and Zhao M. (2019) Impacts of natural and human-induced hydrological variability on particulate organic carbon dynamics in the Yellow River. *Environ. Sci. Technol.* **53**, 1119–1129.

Yuan D., Zhu J., Li C. and Hu D. (2008) Cross-shelf circulation in the Yellow and East China Seas indicated by MODIS satellite observations. *J. Mar. Syst.* **70**, 134–149.

Yuan Z., Xing L., Li L., Zhang H., Xiang R. and Zhao M. (2013) Biomarker records of phytoplankton productivity and community structure changes during the last 14000 years in the mud area southwest off Cheju Island, East China Sea. *J. Ocean Univ.* **12**, 611–618.

Yuan Z., Xiao X., Wang F., Xing L., Wang Z., Zhang H., Xiang R., Zhou L. and Zhao M. (2018) Spatiotemporal temperature variations in the East China Sea shelf during the Holocene in response to surface circulation evolution. *Quat. Int.* **482**, 46–55.

Zhang Y., Xiao X., Liu D., Wang E., Liu K., Ding Y., Yao P. and Zhao M. (2020) Spatial and seasonal variations of organic carbon distributions in typical intertidal sediments of China. *Org. Geochem.* **142** 103993.

Zhong F., Xiang R., Yang Y. and Zhao M. (2018) Evolution of the Southern Yellow Sea Cold Water Mass during the last 7 kyr from benthic foraminiferal evidence. *Sci. China-Earth Sci.* **61**, 1406–1418.

Zhou L., Liu J., Saito Y., Zhang Z., Chu H. and Hu G. (2014) Coastal erosion as a major sediment supplier to continental shelves: example from the abandoned Old Huanghe (Yellow River) delta. *Cont. Shelf Res.* **82**, 43–59.

Zhu C., Weijers J. W. H., Wagner T., Pan J.-M., Chen J.-F. and Pancost R. D. (2011) Sources and distributions of tetraether lipids in surface sediments across a large river-dominated continental margin. *Org. Geochem.* **42**, 376–386.

Zong Y. (2004) Mid-Holocene sea-level highstand along the Southeast Coast of China. *Quat. Int.* **117**, 55–67.

Associate editor: Thomas Wagner